Numerical Heat Transfer, Part A: Applications: An International Journal of Computation and Methodology
Publication details, including instructions for authors and subscription information:
http://www.tandfonline.com/loi/unht20

A Fast Algorithm to Predict Cell Trajectories in Microdevices Using Dielectrophoresis

Talukder Z. Jubery [a] & Prashanta Dutta [a]
[a] Mechanical and Materials Engineering , Washington State University , Pullman , Washington , USA
Published online: 02 May 2013.

To cite this article: Talukder Z. Jubery & Prashanta Dutta (2013): A Fast Algorithm to Predict Cell Trajectories in Microdevices Using Dielectrophoresis, Numerical Heat Transfer, Part A: Applications: An International Journal of Computation and Methodology, 64:2, 107-131

To link to this article: http://dx.doi.org/10.1080/10407782.2013.773780

Numerical Heat Transfer, Part A, 64: 107–131, 2013

ISSN: 1040-7782 print/1521-0634 online
DOI: 10.1080/10407782.2013.773780

Taylor & Francis
Taylor & Francis Group

A FAST ALGORITHM TO PREDICT CELL TRAJECTORIES IN MICRODEVICES USING DIELECTROPHORESIS

Talukder Z. Jubery and Prashanta Dutta
Mechanical and Materials Engineering, Washington State University, Pullman, Washington, USA

Prediction of accurate trajectories of biological particles is necessary for efficient design of microdevices for dielectrophoretic manipulation. Due to simplicity, a point-based method is generally used to simulate particle trajectory, but a point-based method provides significant distortion from the actual path when particle size is comparable to the device characteristic dimension. This article reports an efficient numerical model which can overcome these drawbacks of a point-based method and can be used for accurate predictions of particle trajectory. This model is formulated on a distributed Lagrange multiplier based fictitious domain (FD) approach for flow field and motion of particles, and the multi-domain method for electric potential. In this study, the dielectric forces are calculated from the Maxwell stress tensor. The accuracy of the proposed methods are validated separately with two test problems: terminal velocity of a particle in a stationary fluid while it is pulled with a constant force, and dielectrophoretic force acting on a particle when it is placed in between two planar electrodes. The capability of the proposed model is demonstrated by simulating trajectories of two biological particles (cells) of the same geometry and size but different dielectric properties in a microdevice. The effects of frequency, particle-particle initial separation distance, and particles' relative position are investigated. Numerical results indicate that this model can capture the physics of particle manipulation better than the conventional point-based method. Moreover, this algorithm reduces the computational time significantly, which is a major bottleneck in 3-D simulation.

1. INTRODUCTION

Dielectrophoresis (DEP) refers to the motion of polarized particles suspended in a medium due to a spatially nonuniform electric field. In DEP, the direction of this particle motion depends on polarization properties of the particle and the surrounding medium. For example, when a particle is more polarizable than the medium, the net force experienced on the particle act towards the higher electric field; this process is called positive DEP (Figure 1*a*). On the other hand, when a particle is less polarizable than the medium, the net force works towards the lower electric field and this algorithm process is known as negative DEP (Figure 1*b*).

In recent years, dielectrophoretic forces have been used to manipulate biological entities (e.g., red blood cell, white blood cell, platelets, cancer cell, bacteria, yeast etc.). These forces have been used for trapping, sorting, focusing, filtration, patterning, and

Received 24 July 2012; accepted 12 January 2013.
The research was supported by Washington State University.
Address correspondence to Prashanta Dutta, Mechanical and Materials Engineering, Washington State University, Pullman, WA 99164, USA. E-mail: dutta@mail.wsu.edu

NOMENCLATURE

D	height of computational domain, m
$D[\vec{V}]$	rate of strain tensor, 1/s
d_h	Indicator function
d	spacing between electrodes, m
$\vec{E}$	electric field, V/m
$\tilde{\vec{E}}$	complex electric field, V/m
$\vec{E}_o$	amplitude of electric field, V/m
$\vec{f}_b$	body force density vector, N/m^3
$\vec{f}_p$	pseudo force density vector, N/m^3
f	frequency, Hz
g	gravitational acceleration, m/s^2
$\vec{H}$	magnetic field, A/m
I	unit tensor
I_p	moment of inertia, kg m^2
L	length of computational domain, m
l_1	location of 1st electrode starting point in x-direction, m
M_p	total mass, [kg]
$\vec{n}$	surface normal vector, m
p	pressure, N/m^2
$\hat{p}$	pseudo pressure, N/m^2
q	net charge density, C/m^3
Re[..]	real part of complex term
R	radius of particles, m
$\vec{r}$	distance vector with respect to center of particle, m
T_M	Maxwell stress tensor, N/m^2
t	time, s
$\vec{V}$	flow field vector, m/s
$\vec{V}_{entry}$	flow field vector at the inlet of main device, m/s
$\hat{\vec{V}}$	pseudo flow field vector, m/s
w	width of electrode, m
W	width of computational domain, m
$\vec{X}$	position vector, m
x	position in x coordinate, m
y	position in y coordinate, m
z	position in z coordinate, m
α	parameter for fully developed flow
β	parameter for fully developed flow
ε	permittivity, F/m
$\tilde{\varepsilon}$	complex permittivity
μ	kinematic viscosity, $m^2 s^{-1}$
ξ	parameter for fully developed flow
ρ	density, kg/m^3
σ	electrical conductivity, S/m
$\tilde{\varphi}$	complex electric potential, V
φ	electric potential, V
φ_o	amplitude of electric potential, V
Ω	computational domain
$\partial\Omega$	computational domain boundary
ω	angular frequency [rad/s]

Subscripts

f	fluid
r	rigid body
s	solid
*	complex conjugate

Superscripts

n	parameter for time level
m	parameter for time level
k	parameter for time level

separation of biological entities suspended in buffer media [1, 2, 3]. In these processes, trajectories of particles are of paramount interest for efficient design of microdevices. For example, in some microdevices, a mixture of particles is separated by levitating them at different heights by dielectrophoretic forces [4]. Efficient positioning of separation channels for different particles also depends on the accurate prediction of particles' levitation height. Until now, most of the work used very simplified calculations to predict particle trajectories. For example, particles' trajectories are predicted based on a model with an isolated particle using the point-dipole [5, 6] approximation. The point-dipole approximation is computationally efficient as the size or the presence of the particle does not need to be considered while solving electric/flow field. However, when the size of the particle is comparable to the device characteristic dimension and/or if a particle is in close proximity to an electrode or another particle, the point-dipole approximation is not accurate. The presence of the particle modifies the overall electric-field distribution and, thus, the dielectrophoretic forces [7, 8]. In such cases, multipolar approximation [9] has been used to obtain better results than

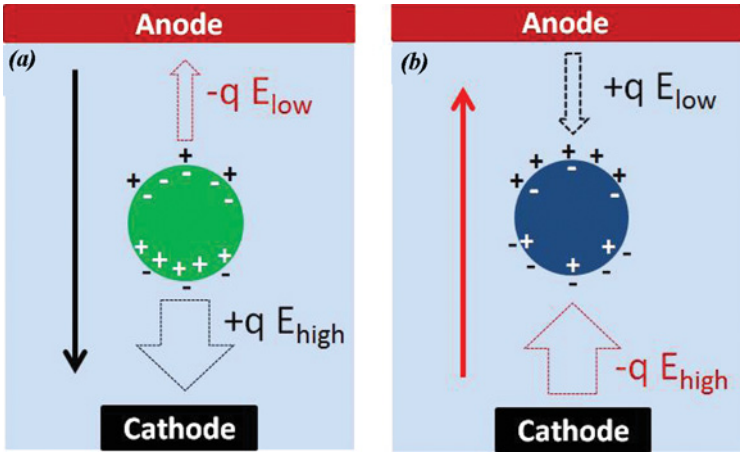

Figure 1. Dielectrophoresis of a particle in a nonuniform electric field created by the electrodes of different lengths. A high electric field region is created close to the bottom electrode and a low electric field is formed close to the upper electrode. (*a*) The particle is more polarizable than the medium and it experiences net force towards the higher electric field (E_{high}) region. This process is known as positive dielectrophoresis; and (*b*) The particle is less polarizable than the medium, and the net force on the particle acts towards the lower electric field (E_{low}) region. This type of particle motion is known as negative dielectrophoresis (color figure available online).

the point-dipole approximation [10]. In this method, the particle under consideration is modeled by a set of multipoles producing the same field distortion caused by the presence of the particle. However, this multipole approximation is only developed for spherical particles, and so far it has been extended to some non-spherical particles in uniform applied electric field only [11, 12].

Biological particles are not spherical; for example, human red blood cells (RBCs) are essentially oblate spheroids with indented sides, while viruses and bacteria often have elongated cigar shapes. Moreover, a nonuniform electric field is generally applied in microfluidic devices, where the size of the particles is comparable to device characteristic dimension. In such a situation, an alternative approach to find dielectrophoretic force is the Maxwell stress tensor (MST) method [9]. This method considers the size and shape of the particle in electric field calculation, and is applicable for any shape and size of particles.

The motion of the particle due to dielectrophoretic force is also affected by the hydrodynamic drag from the surrounding fluid flow. Due to low Reynolds number in such flows, generally, hydrodynamic drag force acting on the particle is calculated by the Stokes drag method [13]. Morgan and Green [5] have determined particle velocity by equating Stokes drag force with dielectrophoretic force. When particles are close to the wall or other particle and are comparable with device size, a correction factor is used along with Stokes drag [14, 15]. However, expression for Stokes drag force is only available for regular shaped bodies (e.g., spheres, ellipsoids, and cylinders) [16], and extension of this method to irregular shaped bodies is not as straightforward. Thus, in such cases, a more appropriate approach is to solve the fluid flow considering the presence of the particle.

There are limited models and numerical works for dielectrophoretic particle manipulation in a microdevice considering the presence of particles, while solving flow field and electric field. A conventional approach is to use unstructured grids that conform to the particle-fluid interface. Ai et al. [17] developed a model using unstructured grids in an arbitrary Lagrangian-Eulerian (ALE) framework to solve flow field, electric field, and particle motion simultaneously. In the ALE framework, an iterative algorithm is used to maintain the particle-fluid interface conditions, and a moving mesh scheme is used to update the interface; mesh regeneration is required when grid becomes distorted. Though this method provides an accurate solution, moving mesh and mesh regeneration increase the computational cost and memory requirements significantly. To reduce the computational tax, numerical schemes have been developed based on fixed grid with a nonconforming particle-fluid interface. In these methods, the particle-fluid interface location and related interface conditions are imposed with model equations so that nonconforming mesh can be implemented [18, 19]. In this case, the fluid and solid equations are solved independently from each other with their respective grids, and re-meshing is not necessary. Several numerical schemes have been reported based on a fixed grid for simulating DEP manipulation of a particle using an immersed electrokinetic finite element method [20] and coupled immersed interface–boundary element method [21]. In the immersed electrokinetic finite element method, the flow and electric fields were solved with the immersed finite element method. On the other hand, in the coupled immersed interface–boundary element method, the flow field was solved with the immersed interface method and the electric field was solved with the boundary element method. In these fixed grid-based methods, a model governing equation is developed by adding an extra force-equivalent term to fluid equations to represent the fluid-particle interface conditions. In these unified fluid equations, the extra forces are satisfied through iterative process or explicit calculation [19, 22]. Recently, Hsu et al. [23] developed an adapted version of distributed Lagrange-multiplier based fictitious domain (FD) model to solve the flow field, and a finite volume method to solve the electric field. In this model, the extra force in the unified fluid equation does not require to be calculated explicitly. Rather, it has been implemented using a momentum conservation principle in the solid domain. Thus, this method is simple and computationally efficient, and it can also be easily implemented to any arbitrary shaped particles. Implementation of this method to device level simulation has not been presented. Device level simulation for dielectrophoretic manipulation requires solving unsteady three-dimensional equations. As a result, more computer memory and time are required for device level simulation. In this article, we have presented an efficient algorithm for device level simulation of DEP which can reduce the computing time significantly. Moreover, this algorithm has been implemented to analyze the path-lines of different cells in a DEP assisted continuous cell separation device.

2. GOVERNING EQUATIONS

In DEP, particles are suspended in a fluid medium, as shown in Figure 2. Thus, we first introduce governing equations for solid and fluid separately. If we consider the fluid is incompressible and Newtonian, the motion of fluid is governed by the Navier-Stokes equation [24].

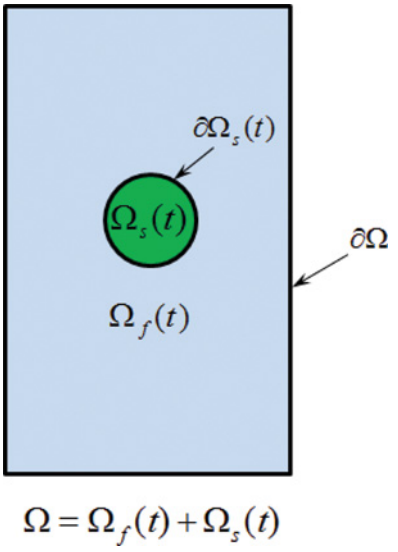

Figure 2. Schematic of the domain considered for presenting the governing equations of particle manipulation. The computational domain (Ω) consists of a solid domain $\Omega_s(t)$ and a fluid domain $\Omega_f(t)$. The entire domain is fixed with respect to time; however, due to motion of particle, both solid and fluid domain are cosidered as a function of time. The interface between the solid and the fluid domain is denoted by $\partial\Omega_s(t)$ and other boundaries are denoted as $\partial\Omega$ (color figure available online).

$$\rho_f\left(\frac{\partial\vec{V}}{\partial t} + (\vec{V}\cdot\vec{\nabla})\vec{V}\right) = -\nabla p + \mu\nabla^2\vec{V} + \rho_f\vec{g} + \vec{f}_{bf} \quad \text{in } \Omega_f(t) \tag{1a}$$

where ρ_f, μ, $\vec{V}$, and p are the fluid density, viscosity, velocity and pressure, respectively, and $\vec{g}$ is the gravitational acceleration. The last term of Eq. (1*a*) is the body force experienced by fluid due to the applied electric field. The incompressibility condition requires a divergence-free velocity field given by the continuity equation.

$$\nabla\cdot\vec{V} = 0 \quad \text{in } \Omega_f(t) \tag{1b}$$

The motion of rigid particle is generally expressed by Newton's equations of motion. However, for the fictitious domain method, the interior of the particle is assumed to be filled with the fluid. A pseudo-body force is introduced over the particle's inner domain to make the fictitious fluid satisfy the rigid body motion. In the distributed Lagrange multiplier method, the pseudo-body force is implemented using rigidity constraint [25]. Thus, the governing equation for the particle motion becomes the following.

$$\rho_s\left(\frac{\partial\vec{V}}{\partial t} + (\vec{V}\cdot\vec{\nabla})\vec{V}\right) = -\nabla p + \mu\nabla^2\vec{V} + \rho_s g + \vec{f}_{bs} + \vec{f}_{ps} \quad \text{in } \Omega_s(t) \tag{2a}$$

with incompressibility and rigidity constraints as,

$$\nabla \cdot \vec{V} = 0 \quad \text{in } \Omega_s(t) \tag{2b}$$

$$D[\vec{V}] = 0 \quad \text{in } \Omega_s(t) \tag{2c}$$

where ρ_s is the particle density, and $D[\vec{V}]$ is the rate of strain tensor which is related to velocity by $D[\vec{V}] = \frac{1}{2}\left(\nabla\vec{V} + (\nabla\vec{V})^T\right)$. $\vec{f}_{bs}$ is the equivalent body force experienced by solid due to applied electric field, and $\vec{f}_{ps}$ is the pseudo force due to rigidity constraint.

Combining Eqs. (1) and (2), the motion for the whole domain (Ω) can be expressed with the following unified equations:

$$\rho\left(\frac{\partial\vec{V}}{\partial t} + (\vec{V}\cdot\vec{\nabla})\vec{V}\right) = -\nabla p + \mu\nabla^2\vec{V} + \rho g + (1-d_h)\vec{f}_{bf} + d_h(\vec{f}_{bs} + \vec{f}_{ps}) \quad \text{in } \Omega \tag{3a}$$

$$\nabla \cdot \vec{V} = 0 \quad \text{in } \Omega \tag{3b}$$

$$\nabla \cdot D[\vec{V}] = 0 \quad \text{in } \Omega_s(t) \tag{3c}$$

$$D[\vec{V}]\cdot\vec{n} = 0 \quad \text{in } \partial\Omega_s(t) \tag{3d}$$

where d_h is the indicator function. The value of d_h is 1 in the solid domain and 0 in the fluid domain. Thus, the expression of density for the unified domain can be given as follows.

$$\rho = (1-d_h)\rho_f + d_h\rho_s \tag{3e}$$

Body force acting on the fluid and solid domains depends on the distribution of the electric field in the domain. The governing equation for the electric field can be derived from the Ampere's Law with Maxwell's correction, and it can be expressed in the frequency domain as follows.

$$\nabla \times H = \sigma\tilde{\vec{E}} + i\omega\varepsilon\tilde{\vec{E}} \tag{4a}$$

where H, ε, and σ are the magnetic field, permittivity and conductivity, respectively, and ω is the angular frequency which is related to applied electric frequency f as $\omega = 2\pi f$. The complex electric field $\tilde{\vec{E}}$ is related to the complex electric potential ($\tilde{\phi}$) by the following.

$$\tilde{\vec{E}} = -\nabla\tilde{\phi} \tag{4b}$$

Taking divergence of Eq. (4*a*), the LHS ($\nabla\cdot(\nabla\times H)$) becomes zero and the equation can be expressed as follows.

$$\nabla\cdot\sigma\tilde{\vec{E}} + i\omega\nabla\cdot(\varepsilon\tilde{\vec{E}}) = 0 \tag{4c}$$

Defining complex permittivity as $\tilde{\varepsilon} = \varepsilon - \frac{i\sigma}{\omega}$, Eq. (4*c*) can be written as follows.

$$\nabla \cdot (\tilde{\varepsilon}\nabla\tilde{\phi}) = 0 \quad \text{in } \Omega \tag{4d}$$

Thus, for unified domain, $\tilde{\varepsilon}$ is the unified complex permittivity which is given as $\tilde{\varepsilon} = d_h \cdot \tilde{\varepsilon}_s + (1 - d_h) \cdot \tilde{\varepsilon}_f$, where $\tilde{\varepsilon}_s = \varepsilon_s - \frac{i\sigma_s}{\omega}$ and $\tilde{\varepsilon}_f = \varepsilon_f - \frac{i\sigma_f}{\omega}$ are the complex permittivity of solid and fluid, respectively.

The electrical body force acting on the solid can be expressed using MST (T_M).

$$\vec{f}_{bs} = \nabla \cdot T_M \quad \text{in } \Omega_s(t) \tag{5a}$$

In most DEP application, frequency of the applied electric field is below 100 MHz. In this case, the electromagnetic wavelength (in meter scale) of the applied field is several orders of magnitude higher than the typical electrode dimension (in micron scale). It implies that the electromagnetic wave's transit time across the system is much smaller than the characteristic time of the system. Thus, using quasi-electrostatic approximation [26], the effect of magnetic field can be neglected [27] and the MST can expressed as [9] follows.

$$T_M = \varepsilon\left(\vec{E}\vec{E} - \frac{1}{2}(\vec{E}\cdot\vec{E})I\right) \tag{5b}$$

Using complex variables formulation, Eq. (5*b*) can be written as follows.

$$\begin{aligned} T_M = {} & \frac{1}{4}\mathrm{Re}(\tilde{\varepsilon})\left((\tilde{\vec{E}}\tilde{\vec{E}}^* + \tilde{\vec{E}}^*\tilde{\vec{E}}) - |E|^2 I\right) \\ & + \frac{1}{4}\varepsilon\left((\tilde{\vec{E}}\tilde{\vec{E}} + \tilde{\vec{E}}^*\tilde{\vec{E}}^*) - \frac{1}{2}(\tilde{\vec{E}}\cdot\tilde{\vec{E}} + \tilde{\vec{E}}^*\cdot\tilde{\vec{E}}^*)I\right) \end{aligned} \tag{5c}$$

where $\tilde{\vec{E}}^*$ is the complex conjugate of $\tilde{\vec{E}}$. Note, that the second term of the right side is an instantaneous part and it will be zero if averaged over time.

In DEP, particle response time scale is much higher than the frequency time scale of the AC electric field. So, averaged electrical body force term is used in this case. The time-averaged body force in the solid domain can be expressed using Eqs. (5*a*) and (5*c*) as follows.

$$\vec{f}_{bs} = \frac{\mathrm{Re}(\tilde{\varepsilon})}{4}\nabla\cdot(\tilde{\vec{E}}\tilde{\vec{E}}^* + \tilde{\vec{E}}^*\tilde{\vec{E}} - \left|\tilde{\vec{E}}\right|^2 I) \quad \text{in } \Omega_s(t) \tag{5d}$$

Similarly, the time-averaged body force on the fluid can be expressed as follows [27]:

$$\vec{f}_{bf} = \frac{1}{2}\mathrm{Re}\left[\left(\frac{(\sigma\nabla\varepsilon - \varepsilon\nabla\sigma)\cdot\tilde{\vec{E}}}{\sigma + i\omega\varepsilon}\right)\tilde{\vec{E}}^* - \frac{1}{2}\left|\tilde{\vec{E}}\right|^2\nabla\varepsilon\right] \quad \text{in } \Omega_f(t) \tag{6}$$

3. COMPUTATIONAL DOMAIN AND BOUNDARY CONDITIONS

Figure 3*a* shows the schematic of a DEP assisted continuous cell separation device considered for this study. The device has three inlets and two outlets, and has two electrodes at the bottom wall. A mixture of biological particles (cells) is fed through the center inlet, while a buffer solution is introduced in the device through two side inlets. It is important to note that the Reynolds number of fluid flow through this device is very small. Therefore, the cells suspended in this flow should maintain their path with fluid flow if there is no electric field. When electric potential is applied across the electrode, a nonuniform electric field is generated in the channel. Since the dielectric property of the cells and the surrounding buffer is different, the nonuniform electric field will cause dielectrophoretic force on the cells

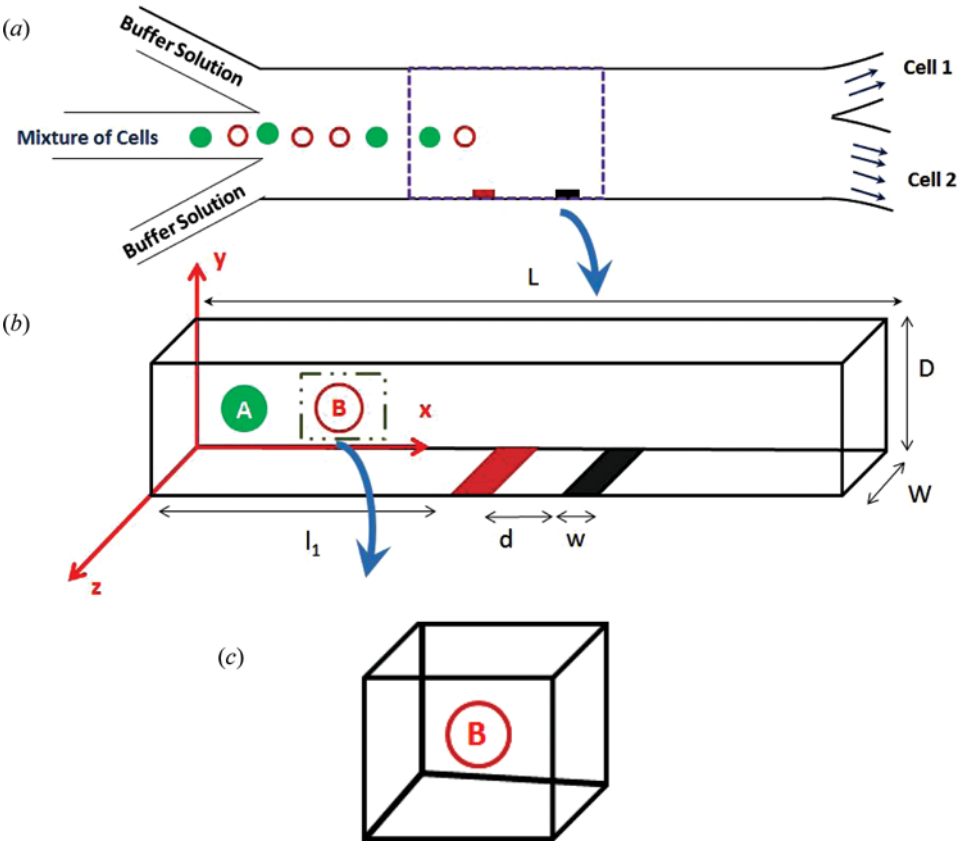

Figure 3. (*a*) Schematic of DEP assisted continous cell separation device. A mixture of cells are introduced at the center of a microchannel by focusing with two streams of buffer. Cells are separated by applying electric potential difference between electrodes at the bottom of the microchannel; (*b*) computational domain considered for both dielectrophoretic and hydrodynamic force calculations. The three-dimensional computational domain has two electrodes of length (*w*) and separation distance (*d*). The length, width, and height of the rectangular channel are (*L*), (*W*) and (*D*), respectively; (*c*) and a subdomain is considered around the particle as shown by a long dash-dot line in the main computational domain (*b*) for a multidomain-based electric field calculation (color figure available online).

and causes them to move. The electric field strength, applied frequency, and the flow rate can be controlled in such a way that cells can be directed to different outlets.

In the above-mentioned device, due to low Reynolds number of the flow, the mixtures of cells maintain their path with fluid flow until in the region close to the electrodes. Moreover, the three inlet streams merge into a single channel, and the flow can be considered to be fully developed at $2W$ away from the inlet [28], where W is the width of the microchannel. The electrodes are generally fabricated more than $2W$ away from the inlet. As fluid flow and cell trajectories are predictable in the device (expect in the electrode region), we considered a calculation domain (Figure 3*b*) which is smaller than the actual device to reduce the computational cost. It includes the area just upstream of the electrodes region to just downstream of that region.

For the unified solid-fluid formulation (Eq. 3*a*), a fully developed flow is considered at the inlet. Considering the same fluid velocity at the three inlets ($\vec{V}_{Entry}$) of the main device (Figure 3*a*), the fully developed flow velocity at the inlet of the computational domain (Figure 3*b*) are obtained from the Stokes equations using the separation of variables technique [29].

$$\vec{V} = \vec{V}_{entry}\left[\frac{48}{\alpha\pi^3}\beta(y,z), 0, 0\right] \tag{7a}$$

where

$$\alpha = 1 - \frac{192W}{\pi^5}\sum_{m=1,3,5}^{\infty}\frac{\tanh(\xi(m))}{m^5} \tag{7b}$$

$$\beta(y,z) = \sum_{m=1,3,5\ldots}^{\infty}(-1)^{(m-1)/2}\left(1 - \frac{\cosh[(2z-1)\xi(m)]}{\cosh(\xi(m))}\right)\frac{\cos(2y\xi(m))}{m^3} \tag{7c}$$

and

$$\xi(m) = \frac{m\pi}{2W} \tag{7d}$$

On the other hand, at the outlet, normal flow with $p = 0$ is considered as boundary condition. For top and bottom walls of the subdomain (Figure 3*b*), no slip and no penetration boundary conditions are prescribed.

As seen in Figure 3*b*, the immersed solid domains are biological cells, which generally consist of thin membrane and cytoplasm. The cytoplasm is comprised of liquid of the same density as the surrounding medium [30]. Thus, we neglect the density variation between solid and particle domains. However, the variations of dielectric properties are significant between solid and fluid domains. For the unified electrostatic equation (Eq. (4*d*)), specified electric potential is considered at electrodes and insulating boundary is considered at all boundaries. The electrical properties of the fluid and solid domain are considered homogenous. In this study, we neglect the effect of Joule heating as the applied electric field is quite small.

4. NUMERICAL TECHNIQUES

The governing equations used to describe the unified fluid-solid motion and the electric potential/field is coupled. The body force terms in the unified fluid-solid motion equation (Eq. (3*a*)) is calculated from the solution of electric potential. On the other hand, the electric potential distribution is affected by the position of solid domains which are obtained from the solution of unified fluid-solid motion. Here an explicit algorithm is used for solving the coupled system. In this study, finite volume method is used to form the algebraic equations for numerical solution. One of the major advantages of the finite volume method is the conservation of the flux of the desired parameter across the domain boundary [31]. Parallel solvers are used to solve the system of equations and an efficient algorithm is used to obtain particle velocity.

The numerical scheme starts with an initial condition for the whole domain. For particular positions and velocities of particles and known fluid velocity at time instant t^n, the following major steps are used to get solution at a new time t^{n+1}.

4.1. Finding Indicator Function d_h in the Entire Domain (Ω)

The solid and fluid domains are distinguished in the entire domain (Ω) by using an indicator function. The indicator function is implemented through the calculation of volume fraction occupied by the solid particle in each control volume. Thus, the indicator function varies smoothly between one and zero in the solid-fluid interfacial control volume, and reduces the difficulties in numerical calculation due to sharp change in properties at the particle boundary.

4.2. Calculate the DEP Force on Particle and Electrokinetic Body Force on Fluid

Dielectrophoretic force is calculated using Eq. (5*d*) from the solution of electric potential. Accuracy of dielectrophoretic force calculation depends on the accuracy of capturing the potential variation across the solid boundary. This is achieved in three steps:

4.2.1. Solving electric potential in entire domain. Eq. (4*d*) is solved for the entire domain with regular grid using the finite volume method.

4.2.2. Solving electric potential in subdomain containing particle. A subdomain is considered around the particle, as shown in Figure 3*c*. The solution from section 4.2.1. is used as a boundary condition for the subdomain, and electric potential is solved using Eq. (4*d*) with a finer grid.

4.2.3. Calculating MST force using volume integration. Dielectrophoretic force on the particle is calculated using Eq. (5*d*). For a spherical particle, the effect of orientation is not important. So, neglecting the effect of torque on particle, MST force can the approximated as follows.

$$\vec{f}_{bs} = \frac{\int_{\Omega_p} \vec{f}_{bs} d\forall}{\int_{\Omega_p} d\forall} \tag{8}$$

For homogenous property of fluid and negligible Joule heating due to applied electric field, the electrokinetic body force term (Eq. (6)) in the fluid domain will be zero.

4.3. Solve for Motion of Fluid and Solid

Fluid and solid motion have been determined by solving the unified fluid-solid problem. As we used an explicit scheme to update the particle, an efficient algorithm is needed to reduce the computational time. To achieve that between original time steps ($t^n \rightarrow (t^{n+1}$), we used intermediate time steps $t^{n+\frac{k}{m}}$ (where m is any integer value and $k = 1, 2, 3 \ldots m-1$) in the fluid and solid motion solver. The dielectrophoretic force acting on the particle domain is constant during these intermediate time steps. As the fluid flow is in the low Reynolds number range, the particle will attain equilibrium velocity only after a few iterations and it will stay the same until the last intermediate time steps. In such situation, for reducing the computational time, we check for the equilibrium velocity at every intermediate steps. If the particle reaches the equilibrium velocity, we consider that velocity as the particle velocity for the next original time level, t^{n+1}.

In the intermediate steps, the fluid-solid motion problem has been solved mainly in two–stage fractional algorithm: the first step is for the entire domain, and the second step is only for the solid domain.

- Solve for pseudo velocity ($\hat{\vec{V}}$) and pseudo pressure ($\hat{p}$) from Eqs. (3*a* and 3*b*) (without pseudo force due to rigidity constraint force). The modified equations are as follows.

$$\rho\left(\frac{\hat{\vec{V}} - \vec{V}^n}{\Delta t} + (\hat{\vec{V}} \cdot \vec{\nabla})\hat{\vec{V}}\right) = -\nabla\hat{p} + \mu\nabla^2\hat{\vec{V}} + (1 - d_h)\,\vec{f}_{bf} + d_h(\vec{f}_{bs}) \text{ and} \quad (9a)$$

$$\nabla \cdot \hat{\vec{V}} = 0 \quad (9b)$$

  Note, that Eqs. (9*a*) and (9*b*) are identical to the original fluid flow Eqs. (1*a*) and (1*b*). So, the obtained velocity and pressure is the solution for fluid domain. Thus, we set

$$\vec{V}^{n+\frac{k}{m}} = \hat{\vec{V}} \text{ and } p^{n+\frac{k}{m}} = \hat{p} \quad \text{in } \Omega_f(t) \quad (9c)$$

  The velocity in the solid domain can be obtained by satisfying rest of Eq. (3) in the next step.
- Solve for $\vec{V}^{n+\frac{k}{m}}$ in particle domain by projecting the flow field onto a rigid body motion satisfying the following equations

$$\rho_s\left(\frac{\vec{V}^{n+\frac{k}{m}} - \hat{\vec{V}}}{\Delta t}\right) = \vec{f}_{ps} \quad (9d)$$

$$\nabla \cdot D[\vec{V}^{n+\frac{k}{m}}] = 0 \quad (9e)$$

$$D[\vec{V}^{n+\frac{k}{m}}] \cdot \vec{n} = 0 \quad (9f)$$

The above equations could be satisfied in an iterative way to solve solid velocity, $\vec{V}^{n+\frac{k}{m}}$. However, here we used a noniterative straightforward way to obtain the solid velocity, developed by Sharma et al. [25]. They argued that imposing conservation of total linear and angular momenta in the solid domain is an alternative way to satisfy Eqs. (9*d*–9*f*). Thus, rigid body motion in the solid domain can be obtained using following equations.

$$M_p \vec{V}r = \int_p \rho_s \hat{\vec{V}} d\forall \tag{9g}$$

$$I_p \omega_r = \int_p \vec{r} \otimes \rho_s \hat{\vec{V}} d\forall \tag{9h}$$

$$\vec{V}^{n+\frac{k}{m}} = \vec{V}r + \omega_r \otimes \vec{r} \tag{9i}$$

where M_p, I_p,$\vec{V}r$, and ω_r are the mass, moment of inertia, translational and angular velocity of particle, respectively, and $\forall$ is the volume. Prior to the above integration, momentum contribution from solid at the solid-fluid interface control volume (which is shared by both solid and fluid) is approximated using the following steps.

- Use linear interpolation from surrounding fluid domain to approximate a velocity ($\hat{\vec{V}}_f$) in the interface control volume.
- Calculate the momentum contribution from the solid using the approximated velocity ($\hat{\vec{V}}_f$) in the following equation.

$$d_h \rho_s \hat{\vec{V}}_s = \rho \hat{\vec{V}} - \rho_f (1 - d_h) \hat{\vec{V}}_f \tag{9j}$$

Set $\hat{\vec{V}} = \hat{\vec{V}} = \hat{\vec{V}}_s$ in the above integration for the interface control volume.

4.4 Check for Equilibrium/Quasi-Steady State and Repeat

Update particle positions with $\vec{V}^{n+\frac{k}{m}}$ using an explicit scheme.

$$\vec{X}^{n+\frac{k+1}{m}} = \vec{X}^{n+\frac{k}{m}} + \Delta t \, \vec{V}^{n+\frac{k}{m}} \tag{9k}$$

Next, calculate the value of indicator function in the whole domain and solve the fluid-solid problem for the next intermediate time level. We also check for the quasi-steady equilibrium velocity of particle at every intermediate time levels. If particle reaches the quasi-steady equilibrium condition, the equilibrium velocity is considered as the particle velocity at t^{n+1} time level. Finally, the particle position is updated with $\vec{V}^{n+1}$ using an explicit scheme.

$$\vec{X}^{n+1} = \vec{X}^{n+\frac{k}{m}} + \Delta t(m-k) \vec{V}^{n+1} \tag{9l}$$

All of the steps are repeated to get particle velocity for the further time levels. The detailed algorithm is shown in Figure 4. A fixed, collocated, finite volume grid is used in the entire domain for numerically implementing the above-mentioned steps. For numerical solution of complex Laplace equation, the linear system of equations is solved using a parallel algorithm (PARMS) developed by Li et al. [32]. PARMS uses flexible GMRES iterative solver with domain decomposition based parallel preconditioners. In our case, we used Block Jacobi as parallel preconditioner and algebraic recursive multilevel solver (ARMS) as local preconditioner with relative error 1e-8. In the subdomain, the complex Laplace equation is solved with Paridso direct solver [33]. The flow field in fluid-solid domain is solved with the Chorin-type projection method [34]. The first order explicit Euler-method is used for time discretization. The pressure Poisons equation is solved using the bi-conjugate gradient stabilized method (BiCGSTAB) with domain decomposition based parallel Jacobi preconditioner [35]. The above algorithm provides the following advantages.

- For dielectrophoretic force calculation, the electric potential variation in the solid-fluid interface needs to be captured accurately. Generally a single domain with fine grid in the particle and particle-fluid interface is used to solve electric potential. The fine grid increases the memory requirements with the increase in number of particles in the domain. On the other hand, using a multi-domain

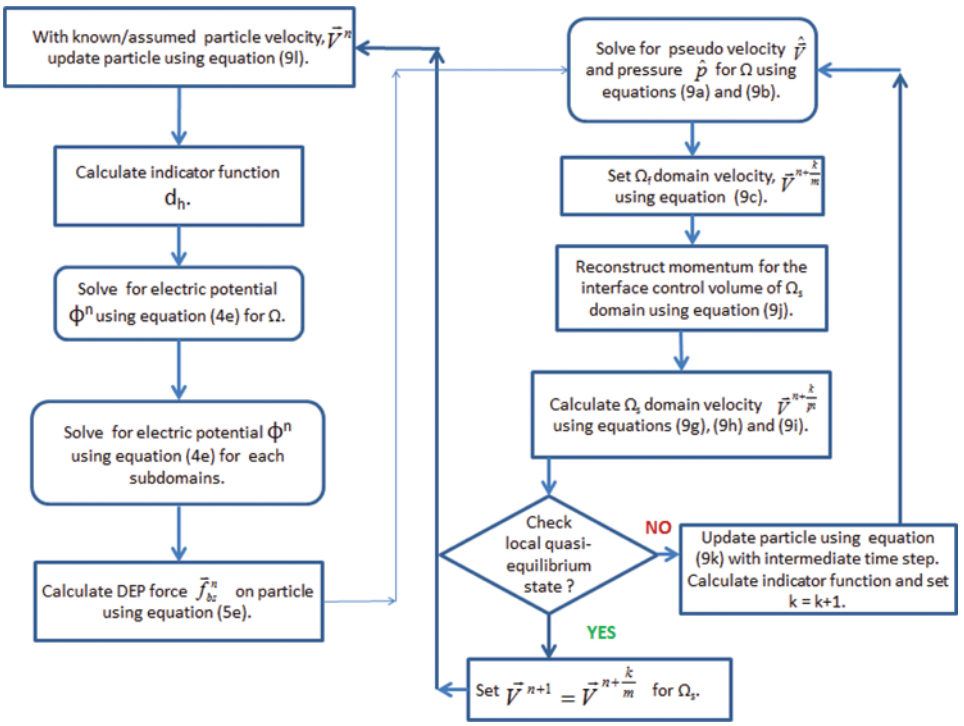

Figure 4. A Fast algorithm for implementing the proposed dielectrophoretic-based particle manipulation process in a microfluidic device (color figure available online).

approach, we observed the same accuracy in numerical results by decomposing the single domain problem into a main domain and subdomain(s) problem for a particle or a group of particles if they are very close to each other. A regular grid is used for the main domain; however, a fine grid is used for the subdomain problem to capture the electric potential variation. As the main domain and subdomain problems are solved separately, it requires less memory than the conventional approach.

- Solving solid-fluid motion with intermediate time steps and stopping at the equilibrium conditions reduce the computing time significantly. In existing algorithms, numerical simulations are performed for all intermediate time steps. The size of the intermediate time step is generally constrained by several factors, which depends on stability of the algorithm/solver used. For example, in the explicit Chorin type projection method, it depends on the Reynolds number of the flow and normalized value of grid size [36], whereas it depends on the stiffness value of the solid domain in an immersed boundary based unified domain solver [37]. Thus, due to the restriction of smaller time steps, performing all of the intermediate time calculations require significantly more time than the proposed algorithm. For example, if we consider 1 μm grid size for a 40 μm characteristic dimension, then for a flow of $\mathrm{Re} = 0.016$, the biggest time step can be ~ 0.167 μs. So, to achieve results at 10 μs it requires about 60 time steps. However, we observed the equilibrium velocity within $\sim$1 μs and it required only 6 intermediate time steps. Thus, the proposed algorithm reduces the computational time than the existing approach.

5. MODEL VALIDATIONS

The above algorithm and formulation are validated for two different cases: one for dielectrophoretic force calculation and the other for particle rigid body motion. Dielectrophoretic force calculation for a particle is compared with the experimental results published by Demierre et al. [4]. They used a microdevice with a set of interdigited liquid electrodes of 56 μm width and 56 μm inter-electrode spacing. A voltage difference of 25 $V_{p\text{-}p}$ was applied between electrodes with frequency 2 MHz, and the dielectrophoretic force was measured on 5.14 μm diameter polystyrene beads which are suspended in buffer. We simulated the experimental setup by replacing the liquid electrodes with regular metal electrodes, and an equivalent applied voltage difference is considered between the electrodes. The equivalent voltage is calculated from the analytical expression presented in the same experimental work [4]. Figure 5 shows the numerically predicted normalized dielectrophoretic force acting on a particle placed at different locations on the axis of symmetry between the electrodes. For comparison, experimental results are also presented; our numerical results are in excellent agreement with the experimental values except very close to the electrodes. The deviation is expected as in the liquid electrodes the equipotential surface defining the opening is not flat, but curved such that the field gradients close to liquid electrodes are somewhat less pronounced than for metal electrodes [4]. However, when the experimental results are compared with point dipole based calculation, the deviation is much higher.

For unified solid-fluid solver validation, we consider that a single, neutrally buoyant, rigid sphere is pulled with a constant force in a rectangular cross-section

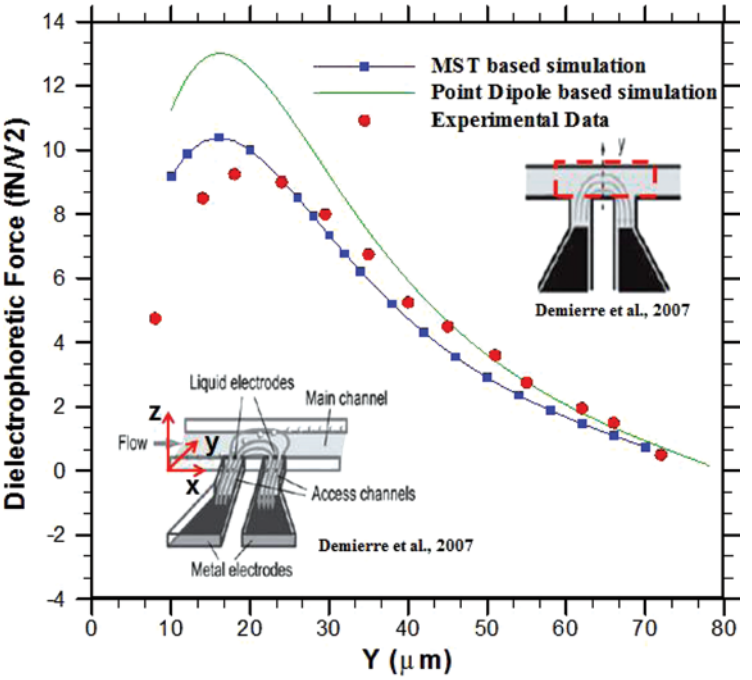

Figure 5. Schematic of experimental set up (bottom left) and dielectrophoretic force acting on a 5.16 μm particle with electrical conductivity 8e-4 S/m and relative permittivity 3.5 at the middle of two electrodes (as in the figure at the top right). The red dotted lines indicates the region considered for numerical simulation. Here, $\sigma_m = 1.4\text{e-}1$ S/m, $\epsilon_m = 80\epsilon_0$, $L = 300\,\mu$m, $W = 20\,\mu$m, $D = 80\,\mu$m, $d = 56\,\mu$m, $w = 56\,\mu$m, and $f = 2$ MHz. Uniform grid of 0.5 micron and 0.1 micron have been used for computational domain (Fig. 3(b)) and subdomain (Fig. 3(c)), respectively (color figure available online).

channel, as shown in Figure 6. Generally, the fluid flow created by particle motion in the microchannel is in the low Reynolds number ($\ll$1), i.e., inertial force is negligible compared to viscous force. In this case, particle terminal velocity can be calculated by equating the applied pulling force to resisting viscous drag. Using analytical expression of Stokes viscous drag for a sphere in an infinite medium, the terminal particle velocity can be found $\sim$140 μm/s and the corresponding Reynolds number is 3.6e-4. This terminal velocity is used to find the normalized particle velocity in the computational domain. Figure 6 shows the normalized particle velocity at different times. It is clear that the terminal velocity of the sphere obtained from our numerical solution is in agreement (within $\sim$95%) with the analytical result. These slight variations ($\sim$5%) can be attributed due to increased drag coefficient on the particle in the presence of wall for the case considered in the numerical simulation.

6. RESULTS AND DISCUSSION

The primary objective of this work is to develop a numerical tool to investigate the physics for particle movement in a liquid under dielectrophoretic force in a microdevice. To demonstrate the capability of our proposed numerical tool, we have selected a microdevice to separate two types of particles: particles A and B. Both

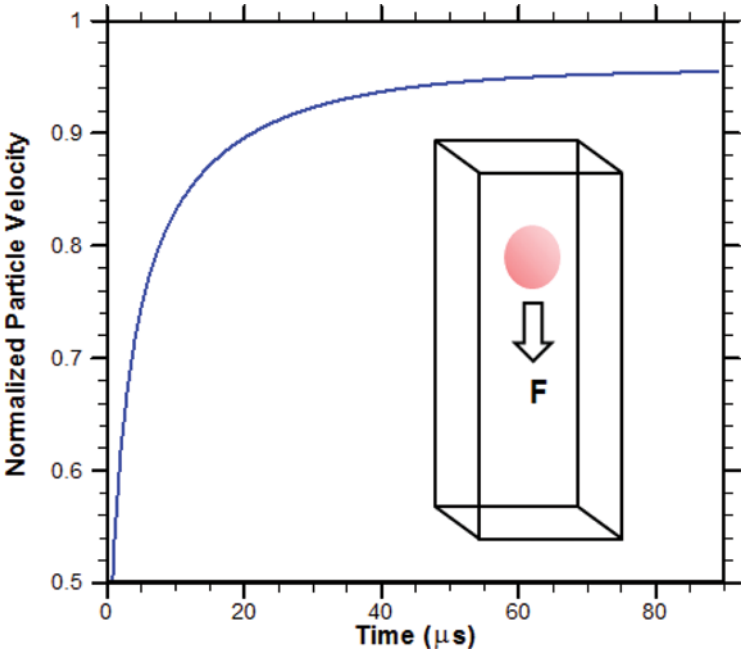

Figure 6. Velocity of a neutrally buoyant 5.16 μm diameter particle pulled through a medium (viscosity 1e-3 Pa-s and density 1000 kg/m^3) inside a square microchannel of width 40 μm. A constant pulling force F = 6.93 pN acting in the downward direction. The velocity is normalized with terminal velocity obtained from the analytical expression of Stokes viscous drag model (color figure available online).

particles' geometry resembles that of a RBC, but they have different dielectric properties. The properties of particles A and B are given in Table 1, along with relevant properties of the background buffer.

In a micro-device, the trajectories of particles depend on a number of parameters, such as applied voltage, frequency, and dielectric properties of particles and surrounding medium. When the particle is more polarizable than the buffer medium ($|\tilde{\varepsilon}_s| > |\tilde{\varepsilon}_f|$), positive DEP attracts the particle to high electric-field region. On the other hand, if the medium is more polarizable ($|\tilde{\varepsilon}_s| < |\tilde{\varepsilon}_f|$, negative DEP repels the particle away from high electric-field region. Generally, for a specific cell and surrounding medium, the permittivity and conductivity are constant. So, the only control parameter is the applied AC frequency to manipulate cell polarization behavior, and thus the type of dielectrophoretic force (positive/negative) acting on the cell. However, the particle proximity with another particle or with the wall can

Table 1. Electrostatic properties of particle A and B and the background buffer

	Conductivity (S/m)	Permittivity (F/m)
Particle A	1.2e-2	3.5e-8
Particle B	6.0e-2	6.5e-8
Buffer	8.67e-2	7.08e-10

also contribute in the particle trajectory. Here, we have presented the effects of frequency, inter particle separation distance, and particle's entry position in the main channel to study the particle's trajectory.

6.1. Effect of Applied Electrical Frequency on Particle's Trajectory

In this section, we present the effect of applied frequency on the particle's trajectory for an applied electric potential difference of 10 $V_{p\text{-}p}$. At first, we consider only one particle in the system, either particles A or B, along the center of the domain (at $x = 25\,\mu m$). We calculated the dielectrophoretic force based on the MST method. However, as there is no interaction between the particles and it is spherical, rather than doing the full scale numerical model we used a Stokes drag-based calculation. This simplification may cause a slight discrepancy from the actual particle trajectory; however, it provides a qualitative trajectory for a single particle to select the required frequency for separation of particles. The simplification also reduces the computation time as it does not require solving the fluid flow. To implement that a parabolic flow profile is considered all over the domain for the buffer flow and particle velocity is calculated by equating the Stokes drag with the dielectrophoretic force.

We studied the particle's trajectories in our system for the following frequencies: (1) 1 MHz, (2) 350 kHz, and (3) 100 kHz. The corresponding absolute value of complex permittivity of particles and buffer medium are presented in Table 2. For the first case, both particles' absolute value of complex permittivity is higher than that of surrounding medium. So, both particles will experience positive DEP and travel towards the edge of the electrode, where the electric field is higher. If there is no external flow, they will attach to the edge of the first electrode. However, when there is an external flow they might move from the edge of the electrode and get trapped in between the electrodes. The trapping positions of two particles will be different, as trapping location depends on the relative magnitude of horizontal and vertical forces acting on a particle. A particle will be trapped if the horizontal force acting on the particle is negligible compared to the vertical force. Both hydrodynamic and dielectrophoretic forces have contribution in the horizontal force, but only dielectrophoretic force contributes in the vertical force. The hydrodynamic drag force is the maximum at the middle of the channel, and it decreases towards the wall due to the parabolic velocity profile, whereas, dielectrophoretic force becomes stronger when the particle approaches the edge of the electrodes.

Figure 7*a* shows that both particles' trajectories are initially straight along the x-axis due to negligible dielectrophoresis force compared to hydrodynamic force. However, as the particles travel and progress towards the electrode, the value of dielectrophoretic forces increase and particles get some downward direction motion.

Table 2. Modulus of complex permittivity at different frequencies

Frequency	Particle A (F/m)	Medium (F/m)	Particle B (F/m)
1 MHz	3.51e-8	1.38e-8	6.57e-8
350 kHz	3.54e-8	3.94e-8	7.05e-8
100 kHz	3.98e-8	13.79e-8	11.55e-8

For particle B at around $x = 90\,\mu m$, x-directional force on the particle becomes negligible compared to y-directional force and the particle is going to get trapped between two electrodes. However, particle A experiences lower dielectrophoretic force than particle B, due to a lower difference in permittivity between particle and medium. In this case, particle A travels more in the x-direction before it is going to trap around the edge of the second electrode ($x = \sim 110\,\mu m$).

At 350 kHz frequency, particle A will experience negative DEP ($|\tilde{\varepsilon}_s| < |\tilde{\varepsilon}_f|$), and particle B should experience positive DEP($|\tilde{\varepsilon}_s| > |\tilde{\varepsilon}_f|$). Figure 7*b* shows that particle B is going to trap along the edge of the second electrode, and particle A is moving away from the electrodes towards the lower electric field region. After crossing the second electrode, particle A keeps moving at the same height due to dominating hydrodynamic force compared to the weak dielectrophoretic force. It

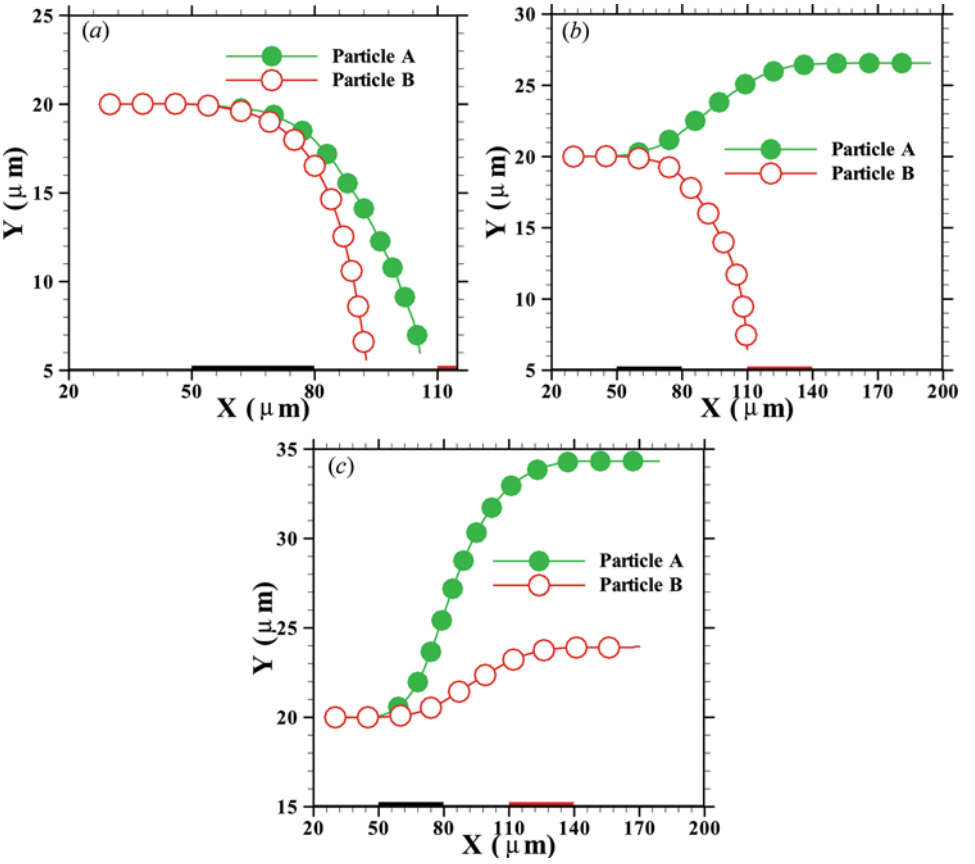

Figure 7. Trajectories of particles A and B in an AC dielectrophoresis for 10 $V_{p\text{-}p}$ at a frequency of (*a*) 1 MHz, (*b*) 350 kHz, and (*c*) 100 kHz. Particles are initially located at $y = 20\,\mu m$ and $z = 20\,\mu m$, but at different x locations. Both particles are 6 μm in diameter. Here, $\vec{V}_{entry}$=200 μm/s, $L = 200\,\mu m$, $W = 40\,\mu m$, $D = 40\,\mu m$, $d = 30\,\mu m$, $w = 30\,\mu m$, and $l_1 = 50\,\mu m$. The red and black rectangles indicate the position of the electrode along the x axis. Electostatic properties of particles and medium are presented in Table 1 (color figure available online).

is also observed that the trapping position of particle B is different because of lower permittivity difference between particle and medium than that in the case of applied frequency 1 MHz.

At 100 kHz frequency, both particles will experience negative DEP as $\left(|\tilde{\varepsilon}_s| < |\tilde{\varepsilon}_f|\right)$. Figure 7*c* indicates that both particles are moving in the positive vertical direction while passing over the electrodes and then keep maintaining the same height. The particle A travelled higher than particle B in the *y*-direction due to a higher difference in absolute value of complex permittivity between particle A and the medium than that of particle B and the medium.

Our numerical results indicate that for frequency 1 MHz and 350 kHz either one or both particles experience positive dielectrophoretic force and might suffer from the particle adherence on the electrode. These trapped particles can interact with untrapped particles and can affect the particle trajectories. In the case of biological cells, the longtime exposure to the applied electric field can also cause cell damage [38]. However, these disadvantages can be overcome using dielectrophoretic levitation on both types of particles, and this can be achieved using negative

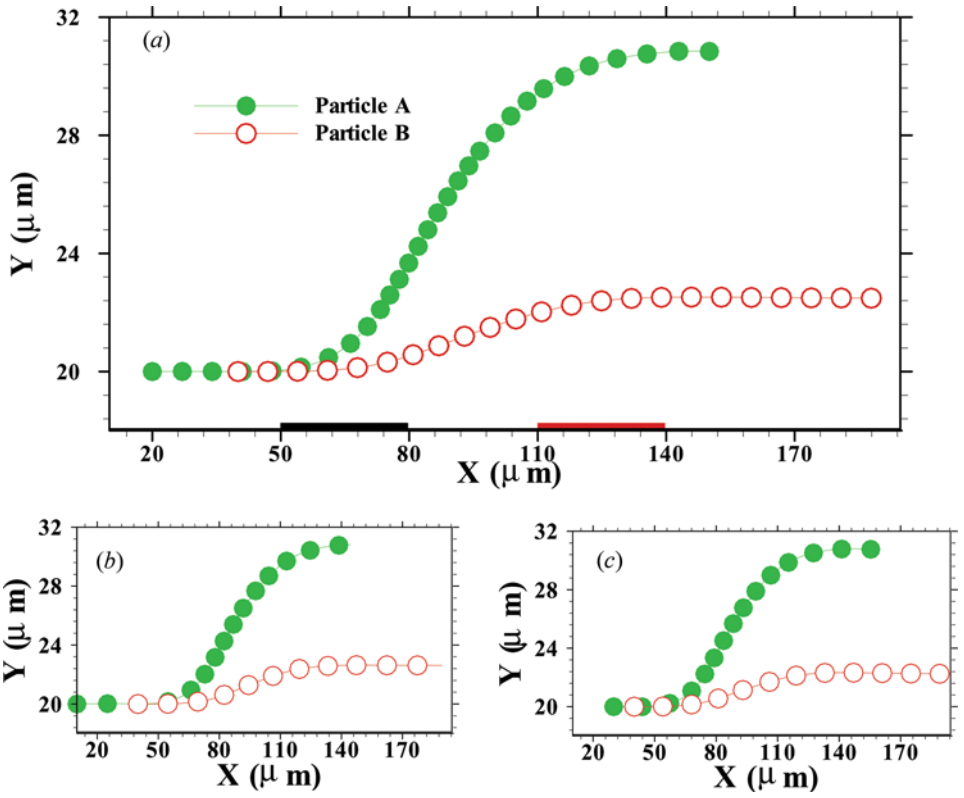

Figure 8. Trajectories of particles A and B with initial separation distance (*a*) 20 μm, (*b*) 30 μm, and (*c*) 10 μm for a 10 $V_{p\text{-}p}$ applied AC potential at a frequency of 100 kHz. Particles are initially at $y = 20$ μm and $z = 20$ μm, but at different x locations. All other simulation conditions are the same as in Figure 7*c* (color figure available online).

dielectrophoretic force on both particles, as shown in Figure 7*c* (f = 100 kHz). This frequency can be used for continuous separation of particles.

6.2. Effect of Initial Particle Distances and Orientation

Based on 100 kHz frequency, we have simulated continuous separation of two particles in the system. Here, we assumed that particles A and B are initially located at the centerline of the device at different x locations. First, we have investigated the effect of initial separation distance between the two particles. Here, the aim was to see how the proximity of one particle affects the other's pathline. We have varied the initial position of particle A, while keeping particle B's position constant at $x = 40\,\mu m$. We studied three cases with particle-particle center to center initial distance 10 R, 6.67 R, and 3.33 R, where R is the radius of the particle. Figure 8*a* shows the particles, trajectories with the initial separation distance between particles being 6.67 R. Numerical results indicate that after passing the electrodes, particle A reaches approximately 30.8 μm height and particle B is at ~22.75 μm, which are smaller than the value got from one particle simulation with the Stokes drag model (Figure 7*c*). This difference can be attributed to the wall effect, which was not included in the Stokes drag model, and/or due to particle-particle interaction in the electric and flow fields. These effects are expected to increase while particles come closer. However, Figures 8*b* and 8*c* show that for initial separation distance of 10 R or 3.33 R, both particles approximately reach the same height as in the case of 6.67 R separation distance. These results suggest that particle-particle interaction in the

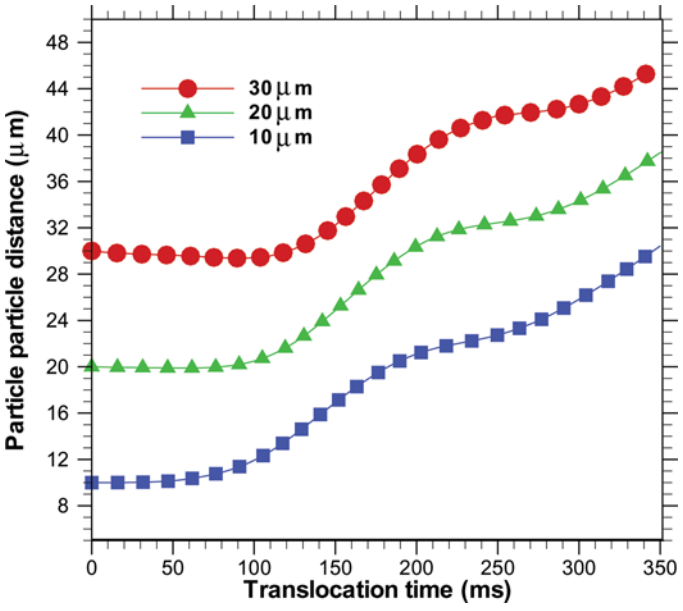

Figure 9. Inter-particle distance as a function of time for various initial separation distances. All other simulation conditions are the same as in Figure 8 (color figure available online).

electric and flow fields is negligible in these three cases, and this is only possible if the particle-particle separation distance increases with time.

Figure 9 shows the inter-particle distance with respect to time for the above three cases. All the three cases show that distance between particles is approximately constant initially, but it keeps increasing with positive slope. The constant inter-particle distance represents the region before the electrode. In this region, electric field is very weak and motion of particles is governed by hydrodynamic force acting on the particle due to surrounding flow of the bulk medium. As both particles maintain the same height in this region, hydrodynamic force due to bulk fluid flow is the same on both of the particles and they move with the same velocity, and the inter-particle distance remains the same.

The positive slope of inter-particle distance can be caused by hydrodynamic force due to bulk flow or dielectrophoretic force due to applied electric field or a

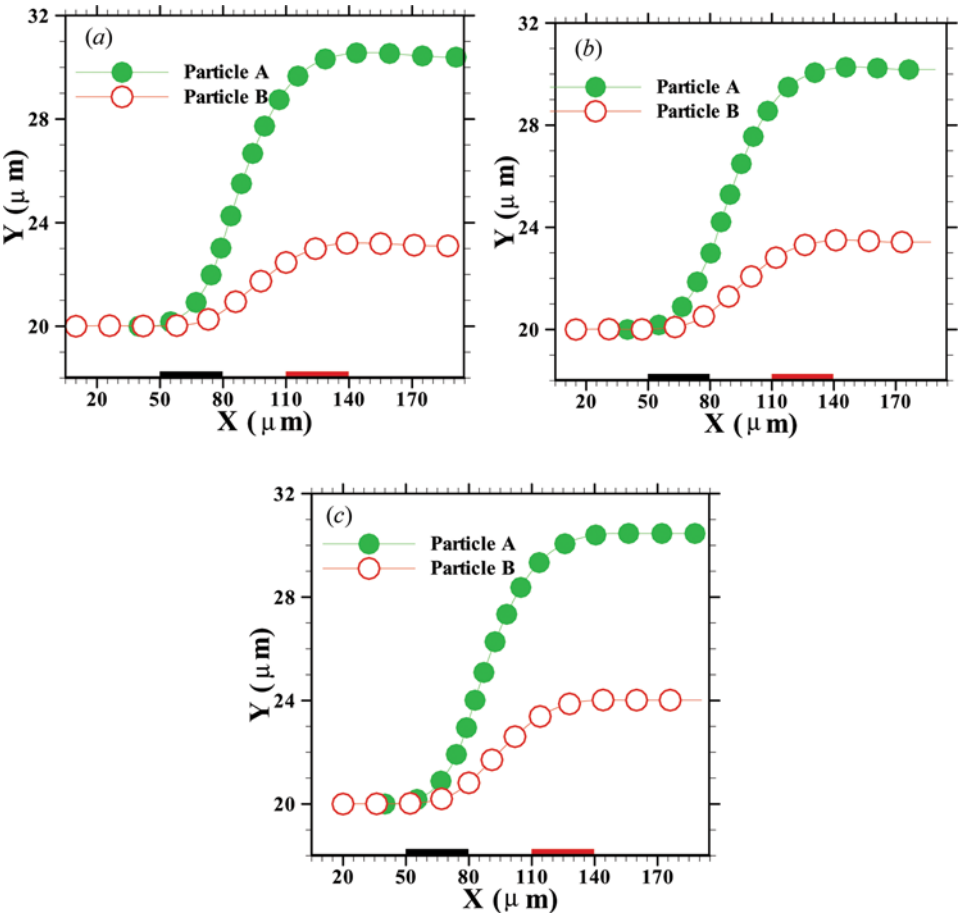

Figure 10. Trajectories of particles A and B with initial separation distance (*a*) 30 μm, (*b*) 25 μm, and (*c*) 20 μm for a 10 $V_{p\text{-}p}$ applied AC potential at a frequency of 100 kHz. Particles are initially at the same $y = 20$ μm and $z = 20$ μm, but at different x locations. All other simulation conditions are the same as in Figure 7*c* (color figure available online).

combination of both. Figure 9 indicates that the positive slope has the highest value at the beginning; it refers to the duration of time while particles are above the region of first electrode or space between two electrodes. Here, both hydrodynamic and negative dielectrophoretic forces provide positive contribution to increase the inter-particle distance. The value of inter-particle distance slope decreases (Figure 9) when particles are in the region above the second electrode. Here, hydrodynamic force has a positive effect but dielectrophoretic force has a negative contribution. The slope magnitude increases again after the electrode region as only hydrodynamic force has a positive contribution and negative DEP has very negligible effect. Figure 9 also reveals that the particle-particle distance increases as time progresses in all the three cases and it diminishes the possibility of particle- particle interaction on the particle trajectories. Though initially the inter-particle distance is within critical range for particle-particle interaction, the effect is quite negligible with respect to other forces acting on the particles.

Next, we study the effect of particles' relative position/orientation on their trajectories. In this case, we have varied the initial position of particle B at $x = 10$ micron to 15 micron and, finally, to 20 micron, while keeping particle A's position constant at ($x = 40\,\mu m$). The three cases refer to particle-particle initial distance 30 μm (10 R), 25 μm (8.33 R), and 20 μm (6.67 R). Figure 10 shows that particle A has levitated around the same height for all the three cases and it is slightly lower than the value found in Figure 8. However, the levitation height of particle B has varied among the cases; it increases as the inter-particle initial distance changes from 10 R to 8.33 R, and then to 6.67 R. This variation can be explained with the Figure 11 and with recent experimental observation of particle-particle dielectrophoretic

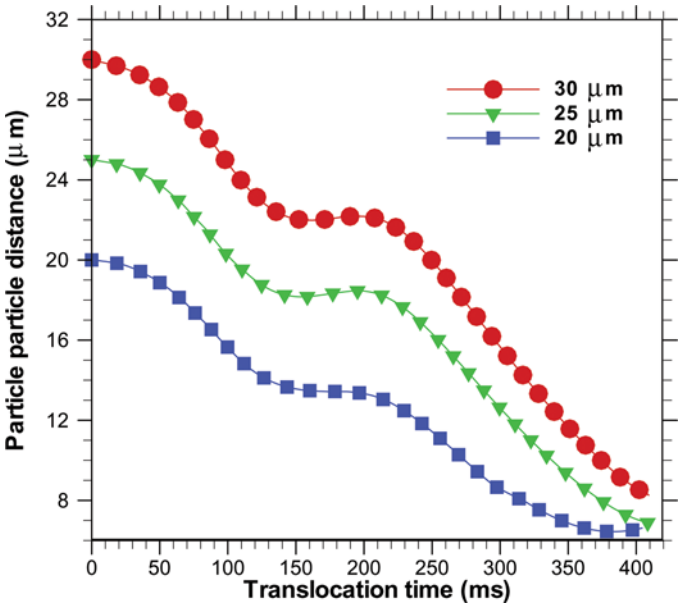

Figure 11. Inter-particle distance as a function of time for various initial separation distances. All other simulation conditions are the same as in Figure 10 (color figure available online).

interactions [39]. Figure 11 reveals that particle-particle distance is decreasing as the time progresses for all the three cases. In this case, the particle-particle interaction force becomes comparable to the other forces acting on the particle. Therefore, we observe variation in levitation height of particle B (Figure 10) for this orientation than the previous case (Figure 8).

8. CONCLUSION

In this article, an efficient algorithm is presented for simulating trajectories of particles in a microdevice under applied AC electric field. The flow field and the motion of particles are solved with a fictitious domain approach based on an adaptive version of distributed Lagrange multiplier method. The electric field is solved using a multi-domain approach, and the dielectrophoretic force acting on the particles are calculated using Maxwell stress tensor. The algorithm is validated separately for particle velocity and dielectrophoretic force calculations. The computational cost in the simulation is reduced (1) by implementing an equilibrium check strategy for fluid-solid motion solver, and (2) by solving Laplace equation for electric potential in two steps by introducing individual subdomains for each particle. This numerical technique is computationally fast and efficient; it can be used as an efficient tool to predict particle trajectories in a microdevice.

This numerical model has great potentials in designing device for dielectrophoretic manipulation of particles including microdevices for separation of infected cells from uninfected ones. We have implemented this algorithm in a microdevice for continuous separation of two particles of same physical dimension but of different dielectric properties. The simulation results indicate that the trajectory of multiparticles is quite different than that of single particle based simulation. In close proximity, particle-particle interaction has a significant effect and can alter the particle trajectories which cannot be captured with traditional point-based method. This numerical method has a shortcoming in accurate tracking of particle-fluid interface due to the use of indictor function in the finite volume based fictitious domain method, However, the proposed fast algorithm can be easily implemented in better interface tracking based numerical methods such as immersed interface, immersed boundary or boundary element methods.

REFERENCES

1. H. A. Pohl, *Dielectrophoresis: The Behavior of Neutral Matter in Nonuniform Electric Fields*, Cambridge University Press, Cambridge, New York, 1978.
2. P. R. C. Gascoyne and J. Vykoukal, Particle Separation by Dielectrophoresis, *Electrophoresis*, vol. 23, pp. 1973–1983, 2002.
3. R. Pethig, Review Article-Dielectrophoresis: Status of the Theory, Technology, and Applications, *Biomicrofluidics*, vol. 4, 2010.
4. N. Demierre, T. Braschler, P. Linderholm, U. Seger, H. van Lintel, and P. Renaud, Characterization and Optimization of Liquid Electrodes for Lateral Dielectrophoresis, *Lab on a Chip*, vol. 7, pp. 355–365, 2007.
5. H. Morgan and N. G. Green, *AC Electrokinetics: Colloids and Nanoparticles*, Research Studies Press, Philadelphia, PA, 2001.

6. T. B. Jones, *Electromechanics of Particles*, Cambridge University Press, Cambridge, New York, 1995.
7. P. Singh and N. Aubry, Trapping Force on a Finite-sized Particle in a Dielectrophoretic Cage, *Physical Review E*, vol. 72, 2005.
8. C. Rosales and K. M. Lim, Numerical Comparison between Maxwell Stress Method and Equivalent Multipole Approach for Calculation of the Dielectrophoretic Force in Single-Cell Traps, *Electrophoresis*, vol. 26, pp. 2057–2065, 2005.
9. X. J. Wang, X. B. Wang, and P. R. C. Gascoyne, General Expressions for Dielectrophoretic Force and Electrorotational Torque Derived using the Maxwell Stress Tensor Method, *J. of Electrostatics*, vol. 39, pp. 277–295, 1997.
10. T. B. Jones and M. Washizu, Multipolar Dielectrophoretic and Electrorotation Theory, *J. of Electrostatics*, vol. 37, pp. 121–134, 1996.
11. N. G. Green and T. B. Jones, Numerical Determination of the Effective Moments of Non-Spherical Particles, *J. of Physics D—Applied Physics*, vol. 40, pp. 78–85, 2007.
12. A. Ogbi, L. Nicolas, R. Perrussel, S. J. Salon, and D. Voyer, Numerical Identification of Effective Multipole Moments of Polarizable Particles, *IEEE Trans. on Magnetics*, vol. 48, pp. 675–678, 2012.
13. R. F. Probstein, *Physicochemical Hydrodynamics: An Introduction*, John Wiley & Sons, New York, 1994.
14. A. J. Goldman, R. G. Cox, and H. Brenner, Slow Viscous Motion of a Sphere Parallel to a Plane Wall—I Motion Through a Quiescent Fluid, *Chem. Engi. Sci.*, vol. 22, 1967.
15. A. Rosenthal, B. M. Taff, and J. Voldman, Quantitative Modeling of Dielectrophoretic Traps, *Lab on a Chip*, vol. 6, pp. 508–515, 2006.
16. A. Holzer and M. Sommerfeld, New Simple Correlation Formula for the Drag Coefficient of Non-Spherical Particles, *Powder Tech.*, vol. 184, pp. 361–365, 2008.
17. Y. Ai, S. Park, J. J. Zhu, X. C. Xuan, A. Beskok, and S. Z. Qian, DC Electrokinetic Particle Transport in an L-Shaped Microchannel, *Langmuir*, vol. 26, pp. 2937–2944, 2010.
18. C. S. Peskin and D. M. McQueen, Modeling Prosthetic Heart Valves for Numerical Analysis of Blood Flow in the Heart, *J. of Computational Physics*, vol. 37, pp. 113–132, 1980.
19. Z. Li, K. Ito, and Society for Industrial, and Applied Mathematics, The Immersed Interface Method Numerical Solutions of PDEs Involving Interfaces, and Irregular Domains, *Frontiers in Applied Mathematics*, vol. 33, Society for Industrial and Applied Mathematics, Philadelphia, PA, 2006.
20. Y. Liu, W. K. Liu, T. Belytschko, N. Patankar, A. C. To, A. Kopacz, and J. H. Chung, Immersed Electrokinetic Finite Element Method, *Inte. J. for Numeri. Methods in Eng.*, vol. 71, pp. 379–405, 2007.
21. D. V. Le, C. Rosales, B. C. Khoo, and J. Peraire, Numerical Design of Electrical-Mechanical Traps, *Lab on a Chip*, vol. 8, pp. 755–763, 2008.
22. R. Glowinski, T. W. Pan, T. I. Hesla, and D. D. Joseph, A Distributed Lagrange Multiplier Fictitious Domain Method for Particulate Flows, *Inte. J. of Multiphase Flow*, vol. 25, pp. 755–794, 1999.
23. H. Y. Hsu, N. Sharma, and N. A. Patankar, An Algorithm for the Simulation of Electrohydrodynamic Rigid Particulate Flows, *Int. J. for Numer. Methods in Biomedical Eng.*, vol. 27, pp. 29–42, 2011.
24. P. Dutta, A. Beskok, and T. C. Warburton, Numerical Simulation of Mixed Electroosmotic/Pressure Driven Microflows, *Numer. Heat Transfer*, vol. 41, pp. 131–148, 2002.
25. N. Sharma and N. A. Patankar, A Fast Computation Technique for the Direct Numerical Simulation of Rigid Particulate Flows, *J. of Computational Physics*, vol. 205, pp. 439–457, 2005.

26. A. Ramos, H. Morgan, N. G. Green, and A. Castellanos, AC Electrokinetics: A Review of Forces in Microelectrode Structures, *J. of Physics D—Applied Physics*, vol. 31, pp. 2338–2353, 1998.
27. M. Zahn, Derivation of the Korteweg-Helmholtz Electric and Magnetic Force Densities Including Electrostriction and Magnetostriction from the Quasistatic Poynting's Theorems, *Proc. Annual Report Conference on Electrical Insulation and Dielectric Phenomena*, pp. 186–189, 2006.
28. I. B. Sprague and P. Dutta, Modeling of Diffuse Charge Effects in a Microfluidic based Laminar Flow Fuel Cell, *Numer. Heat Transfer*, vol. 59, pp. 1–27, 2011.
29. F. M. White, *Viscous FluidFflow*, McGraw-Hill Higher Education, New York, 2006.
30. M. Godin, A. K. Bryan, T. P. Burg, K. Babcock, and S. R. Manalis, Measuring the Mass, Density, and Size of Particles and Cells using a Suspended Microchannel Resonator, *Applied Physics Letters*, vol. 91, paper no. 123121, pp. 1–3, 2007.
31. J. Shim, P. Dutta, and C. F. Ivory, Finite-Volume Methods for Isotachophoretic Separation in Microchannels, *Numer. Heat Transfer A*, vol. 52, pp. 441–461, 2007.
32. Z. Z. Li, Y. Saad, and M. Sosonkina, pARMS: A Parallel Version of the Algebraic Recursive Multilevel Solver, *Numer. Linear Algebra with Applications*, vol. 10, pp. 485–509, 2003.
33. O. Schenk and K. Gartner, Solving Unsymmetric Sparse Systems of Linear Equations with PARDISO, *Future Generation Computer Systems*, vol. 20, pp. 475–487, 2004.
34. A. J. Chorin, Numerical Solution of the Navier-Stokes Equations, *Mathematics of Computation*, vol. 22, pp. 745–762, 1968.
35. M. Griebel, T. Dornseifer, and T. Neunhoeffer, *Numerical Simulation in Fluid Dynamics: A Practical Introduction, Society for Industrial and Applied Mathematics*, Philadelphia, PA, 1998.
36. S. McKee, M. F. Tome, V. G. Ferreira, J. A. Cuminato, A. Castelo, F. S. Sousa, and N. Mangiavacchi, The MAC Method, *Computers & Fluids*, vol. 37, pp. 907–930, 2008.
37. J. M. Stockie and B. R. Wetton, Analysis of Stiffness in the Immersed Boundary Method and Implications for Time-Stepping Schemes, *J. of Computational Physics*, vol. 154, pp. 41–64, 1999.
38. S. Y. Ho and G. S. Mittal, Electroporation of Cell Membranes: A Review, *Critical Reviews in Biotechnology*, vol. 16, pp. 349–362, 1996.
39. H. Hwang, J. J. Kim, and J. K. Park, Experimental Investigation of Electrostatic Particle-Particle Interactions in Optoelectronic Tweezers, *J. of Physical Chemistry B*, vol. 112, pp. 9903–9908, 2008.